Simulation of acoustic reflection and backscatter from Arctic sea-ice

Nicholas P. Chotiros,[1] Gaye Bayrakci,[2] Oliver Sanford,[3] Timothy Clarke,[3] and Angus I. Best[2]

[1] *Applied Research Laboratories, The University of Texas at Austin, Texas 78758, U.S.A.*

[2] *National Oceanography Centre, European Way, Southampton, SO14 3ZH, U.K.*

[3] *Defence Science and Technology Laboratory, Porton Down, Salisbury, Wiltshire, SP4 0JQ, U.K.*

(Dated: 18 May 2023)

Abstract: The rapidly warming Arctic ocean demands new ways to monitor and characterize changes in sea-ice distribution, thickness and mechanical properties. Upward-looking sonars mounted on autonomous underwater vehicles offer possibilities for doing so. Numerical simulations were made of the signal received by an upward-looking sonar under a smooth ice sheet using a wavenumber integration code. Demands on sonar frequency and bandwidth for pulse-echo measurements were analyzed. For typical sea-ice physical properties found in the Arctic ocean, even in highly attenuating sea-ice, there is significant information to be extracted from the received acoustic signal. Discrete resonance frequencies in the signal may be related to leaky Lamb waves, and the frequencies are connected to the ratio of the shear wave speed to thickness of the ice sheet. The periodicity of the multiple reflections of a pulse-compressed signal may be related to the ratio of compressional wave speed to thickness. Decay rates of both types of signals are indicative of the wave attenuation coefficients. Simulations of the acoustic reflection by rough water-ice interfaces were made. Smaller levels of roughness were found to enhance the acoustic signal, while greater levels of roughness are detrimental to the sea-ice characterization process.

I. INTRODUCTION

The purpose of this study is to support the analysis of acoustic characterization of Arctic sea-ice using an upward-looking sonar (ULS), through a modeling-based approach. Engineering and acoustical properties of the Arctic ice, including thickness, compressional and shear wave speeds and attenuations, are of interest. Climate change as a result of higher Arctic temperatures is causing a reduction in the thickness and extent of ice-sheets, which in turn influences the physical properties and therefore acoustic response. Accurately characterizing these changing properties are crucial for understanding the impact of climate change on the Arctic environment. Recent advances in oceanographic long range autonomous underwater vehicles, e.g. Autosub Long Range (Roper *et al.*, 2021), raise the possibility of deploying ULSs for routine in-situ mapping of sea-ice thickness in polar regions given appropriate power management. Satellite based sensing techniques, commonly used to estimate sea-ice thickness, are typically at a much lower resolution of ten's of kilometres (Landy *et al.*, 2022).

A closely associated topic is that of guided waves in elastic plates, since a sheet of ice floating on seawater may be regarded as a fluid-loaded elastic plate. Lamb (Lamb, 1917) derived the equations for waves in an elastic plate in a vacuum, and his name has been associated with a certain type of plate wave ever since. Yu and Tian (Yu and Tian, 2015) presented equations for a plate in which one side is immersed in water and applied it to a steel plate. Georgiades, Lowe, and Craster (Georgiades *et al.*, 2022) characterized leaky waves where the elastic plate is loaded on both sides by two different fluids. Cegla, Cawley and Lowe (Cegla *et al.*, 2005) developed methods to determine material properties based on the quasi-Scholte mode for an aluminum plate. Applied to sea-ice, Moreau et al. (Moreau *et al.*, 2017) modeled and measured plate waves in ice sheets in the laboratory. Serripierri, Moreau, Boué, Weiss and Roux (Serripierri *et al.*, 2022) and Moreau et al. (Moreau *et al.*, 2020) used geophone arrays embedded in ice to invert for properties of naturally formed sea ice off Svalbard using ambient noise as the sound source.

The properties of the Arctic ice sheet have been studied in great detail in the past (Weeks and Assur, 1967). Williams and Francois (Williams and Francois, 1992) made measurements of compressional and shear wave speeds and found a strong dependence on temperature. McCammon and McDaniel (McCammon and McDaniel, 1985), based on several previous measurements, produced empirical expressions for the compressional and shear wave attenuation as functions of temperature, and compared model and measurements of the plane wave reflection coefficient of Arctic ice. More recently, the plane wave reflection coefficient of an Arctic ice sheet of various thicknesses, and a range of elastic properties, has been computed by Hobaek and Sagen (Hobaek and Sagen, 2016). It shows a complicated picture of numerous peaks and valleys of the plane-wave reflection in the acoustic frequency-grazing angle parameter space. The ice-water interface is known to be complex from previous under-ice ULS studies (Wadhams *et al.*, 2006), featuring ice keels and leads in addition to the ice floe.

In practice, an ULS may be used to send a sound pulse to probe the ice. In general, it will have a spherical wave front producing specular and backscatter returns that can be detected by various sensor receiver configurations. This study is an attempt to predict the signals returned by the ice to help guide analysis of field ULS measurements. To this end, a numerical modeling study was performed, using both wavenumber integration and finite element codes, to understand the full acoustic wave field for a representative range of acoustical and physical properties, including perfectly flat and rough ice-water interfaces. In Section II, simulations of the reflected signal from a flat ice sheet are presented, and discrete resonances are identified. In Section III, a brief review of Lamb waves and their connection to the discrete resonances are given. In Section IV, the effect of wave attenuation is briefly explored. In Section V, the effect of roughness at the water-ice interface is explored. Some concluding remarks are made in Section VI.

II. REFLECTION FROM A FLAT ICE SHEET

The reflection of a spherical wave pulse by a smooth ice sheet was simulated using the OASES computational code, which uses a wavenumber integration method (Schmidt, 2011). OASES allows for modeling coupled acoustic-elastic propagation in a horizontally stratified environment. This was performed over a broadband frequency range to study the characteristics of the reflected signal as received at the sonar location (monostatic configuration). In the simulation, the ULS was placed at a depth of 100 m below the ice, as shown in Fig. 1(a). The ice was modeled as a uniform elastic plate with typical elastic properties for Arctic ice, based on published data (McCammon and McDaniel, 1985),(Hobaek and Sagen, 2016), as given in Table I. Each simulation used 131072 wavenumbers, taking approximately 4 hours, for frequencies up to 30,000 Hz on an Intel Macbook Pro. For frequencies up to 5,000 Hz, the run time was approximately 30 minutes.

A 2 m thick sheet of ice was simulated in a cylindrically symmetric environment. The pressure in the water (in Pascals) and the vertical particle velocity in the ice (in μm/s) were computed as functions of position and time. To be able to display them on the same color scale, the vertical velocity was multiplied by a factor of 5. One frame of a video of the simulation, using a signal with a frequency band from 800 to 1600 Hz between -6 dB points, is shown in Fig. 1(b). It shows the incident and reflected acoustic signals in the water, where the position of the sonar is outside of the display area. In the ice, it shows the vertical velocity structure, which consists of alternating upward and downward moving regions. These will be shown to be consistent with Lamb waves (LW). When the upper and lower parts of the ice move in opposite directions, the ice deformation is said to be symmetric. Conversely, when the upper and lower parts move in the same direction, the deformation is asymmetric. The specular acoustic reflection is followed by acoustic energy associated with the Lamb wave, known as the leaky Lamb wave (LLW) signal.

TABLE I. Ice properties used in the wideband OASES simulations.

Parameter	Value
Density (kg/m^3), ρ	900
Compressional wave speed, V_L (m/s)	3600
Shear wave speed, V_S (m/s)	1800
Compressional wave attenuation, a_L (dB/λ_L)	0.216
Shear wave attenuation, a_S (dB/λ_S)	0.648
Thickness, d (m)	2

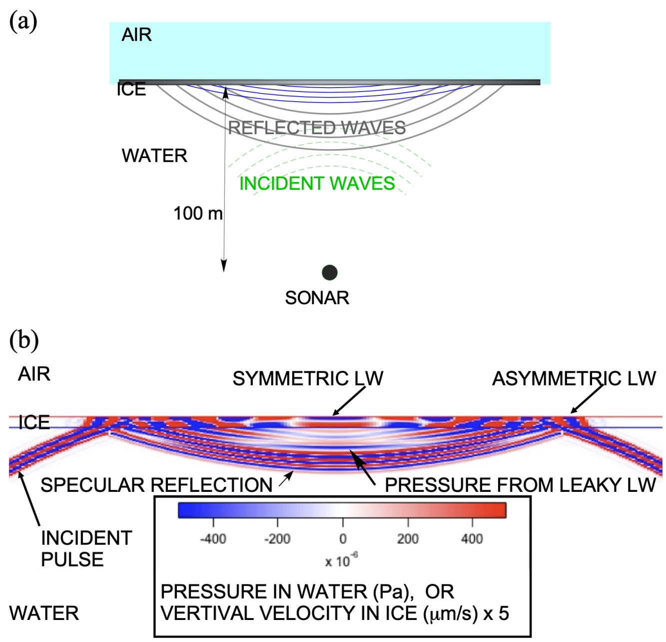

FIG. 1. (a) Illustration of an upward-looking sonar (ULS) under Arctic ice. (b) A representative image of the acoustic pressure in the water and the vertical particle velocity in the ice illustrating the presence of the Lamb wave (LW) in the ice of a broadband signal spanning the frequencies between 400 and 2000 Hz. (color online) The movie MM1 shows the full sequence. This is a file of type "mp4" (3.7 Mb).

Not all waves in an elastic plate can leak or radiate acoustic waves. The conditions for leakage are dependent on the speed V of the interface or plate wave and the angle a of the radiated acoustic wave, as well as the sound speed c_o in the water. They must follow the Bragg condition, as illustrated in Fig. 2 and defined by Eq. (1),

$$sin(a) = \frac{c_o}{V} \tag{1}$$

From this simple equation, it is evident that leakage or radiation can only occur if the interface wave is supersonic, i.e. $V > c_o$. Furthermore, leakage occurs in the normal (vertically

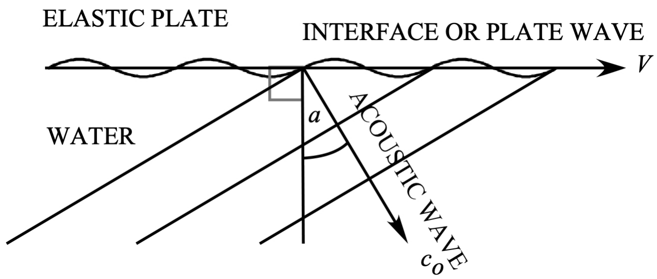

FIG. 2. The condition for an interface or plate wave to radiate acoustic energy into the water. a is the angle of the radiated wave, V and c_o are the phase speeds of interface (or plate) and in water acoustic waves.

downward, $a = 0$) direction as V tends to infinity. This is a rather important result because it simplifies the theoretical model substantially. It is also important because, under these circumstances, the dispersion curves of an elastic plate in a vacuum are indistinguishable from those of a plate that is in contact with water on one side, as shown in Fig. 5 of Moreau et al. (Moreau *et al.*, 2017). A proof is provided in the Appendix. This allows the equations for an elastic plate in a vacuum (Lamb, 1917) to be used, instead of the more cumbersome equations for a plate that is in contact with water (Yu and Tian, 2015).

A number of band limited impulses were simulated to demonstrate the features of the reflected signal. Their spectral windows are shown in Fig. 3, with the computed responses for each band limited simulation shown in Fig. 4.

Reflections from the top and bottom interfaces of the ice, as well as a few multiples, associated with the compressional wave within the ice, are detectable in the highest frequency signals, which have the widest bandwidths (Fig. 4 - A). In the region of 800 Hz and to a lesser extent 400 Hz, a ringing is observed in the signal that is identified as a Lamb wave

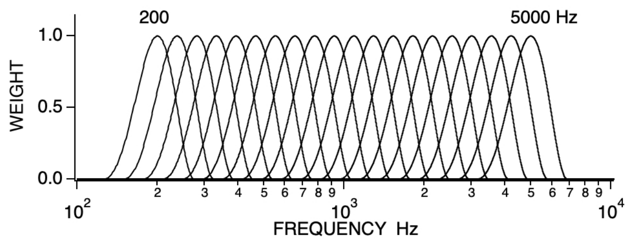

FIG. 3. The spectral windows of 20 band limited signals, logarithmically separated in the frequency domain, that were simulated.

related signal (Fig. 4 - B and C). These are going to be the main focus of this study. To ensure that B and C are indeed Lamb wave effects, another set of simulations were performed with the shear speed in the ice set to zero, as shown in the red dashed line in Fig. 4. The difference between these two sets of simulations highlights the presence of Lamb waves, and their dependence on the shear speed of the ice. The Lamb waves that contribute to the received sonar signal are called leaky Lamb waves (LLW) because they radiate or leak acoustic energy back into the water.

A simulation, using a single wideband signal spanning the band from 50 to 5000 Hz, is used to demonstrate that the main features of the reflected signal should be detectable in a practical environment. The spectrogram of a signal received at an omnidirectional hydrophone in response to a matched-filtered linear chirp pulse of source level (SL) 195 dB re 1 μPa at 1 m, with a time-bandwidth product of 500, emitted from a co-located omnidirectional source, is shown in Fig. 5(a). The signal pulse length is 0.1 s, which is comfortably shorter than the two-way travel time. The ripple in the main spectral ridge (A), with a period of 900 Hz, is due to the multiple reflections of the compressional wave within the ice. The LLW resonances (B, C and D) are detectable above the lowest level in

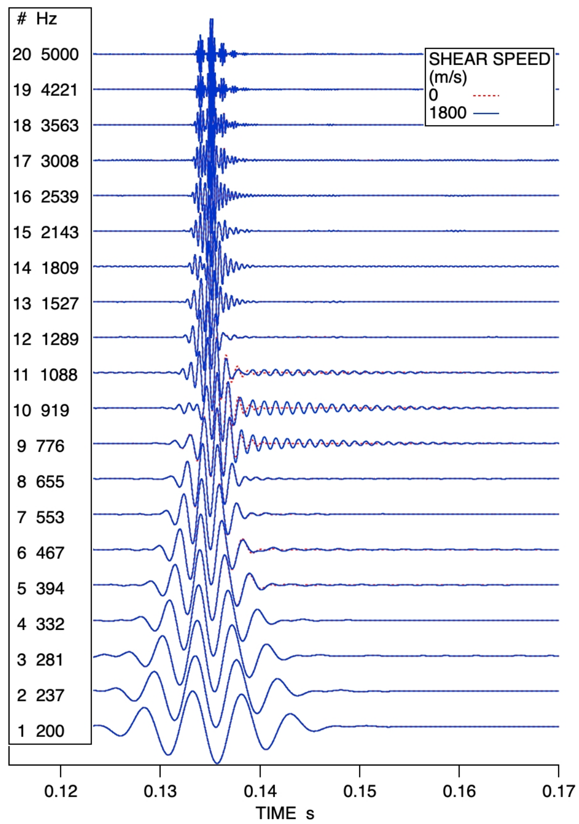

FIG. 4. Responses generated by the band-limited signals from the ice and a liquid ice in which the shear speed is set to zero (red). A: Reflections of the compressional wave from the top and bottom of the ice. B and C: Leaky Lamb wave resonances (color online).

the color scale, which is 90 dB re 1 μPa^2/Hz. The last (D) is not clearly visible in Fig. 4 and it may be argued that the spectrogram is more sensitive than a collection of narrowband signals. Within the frequency band considered, the spectrum level of ambient noise at sea state 5 is 70 dB re 1 μPa^2/Hz or less (Discovery of Sound in the Sea, 2023), which is 20 dB below that of the lowest level in Fig. 5(a). Therefore, the LLW resonances should be easily detectable under most ambient noise conditions. Better performance could be achieved with a directional receiver.

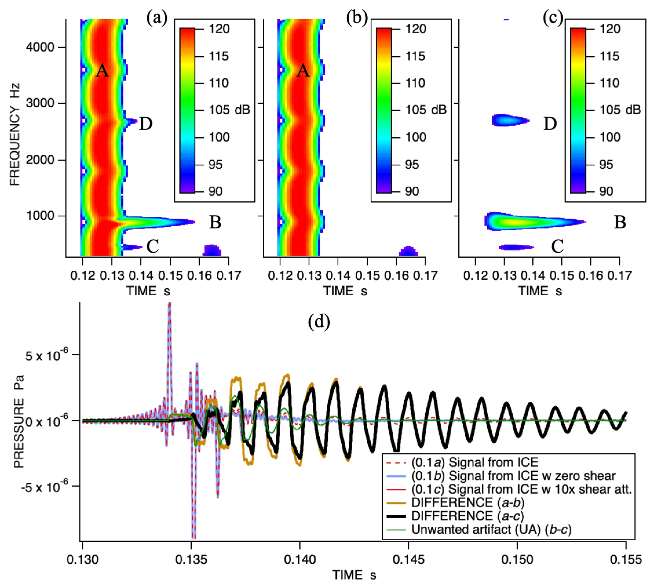

FIG. 5. (a) Spectrogram of the simulated received signal at an omnidirectional hydrophone 100 m below a 2 m thick ice sheet, in response to a matched-filtered linear chirp pulse of source level (SL) 195 dB re 1 μPa at 1 m, and a time-bandwidth product of 500, emitted from a co-located omnidirectional source. The 900 Hz period ripple (A) in the main ridge along the frequency axis is due to multiple bounces of the compressional wave within the ice. The leaky Lamb wave (LLW) resonances appear as ringing decay tails (B, C, and D). (b) The same simulation but with the shear wave speed in the ice set to zero. It has all the compressional wave multiples, but none of the LLW resonances. (c) The spectrogram of the isolated LLW signal, generated by coherently subtracting a simulation in which the shear attenuation is increased by a factor of 10. It captures the LLW resonances while rejecting the compressional reflections, with negligible unwanted artifact (UA). (d) The reflected acoustic signal from the ice (a), ice with zero shear speed (b), and ice with 10 times the shear attenuation (c), all reduced by a factor of 10. The differences $(a - b)$ and $(a - c)$. The unwanted artifact (UA) calculated as $(b - c)$. (color online). Movies MM2 and MM3 show the acoustic pressure in the water and the vertical particle velocity in the ice in the modes labeled B and C. The files are of type "mp4" (1.7 and 1.3 Mb)

The spectrogram in Fig. 5(a) is clearly dominated by the multiple reflections of the compressional wave within the ice (A), and it would be advantageous if the LLW signals (B, C, and D) could be separated out. The signals in Fig. 4 suggest that coherently subtracting the reflected signal from ice with zero shear speed, from that of ice with the proper wave speeds, could be a way to isolate the LLW signal. The spectrogram of the reflected wide-band signal from ice with zero shear speed is shown in Fig. 5(b). It appears to have the same compressional wave reflections but without the LLW signals. The reflected acoustic signals, labeled (a) and (b), and their difference $(a-b)$ are shown in Fig. 5(d). The reflection signals (a) and (b) are reduced by a factor of 10 in the figure to allow greater detail to be seen in the smaller difference signal. An infinite plane wave in water, impinging on a flat water-ice interface at normal incidence, does not excite the shear wave. In that ideal case, the shear speed has no effect on the reflection/transmission coefficient. In this study, the incident wave is a spherical wave, which may be considered as a spectrum of plane waves. At the initial point of contact of a spherical wave, the wave front is locally normal and almost planar. Thus, the difference signal $(a - b)$ at the first reflection is small, as shown in Fig. 5(d). At later times, as the contact area grows wider, the deviation from a normal plane wave increases, and the reflection/transmission discrepancy grows accordingly. This can be seen in $(a - b)$ as a stepwise growth with each multiple reflection. This is an unwanted artifact (UA) caused by setting the shear wave speed to zero. It reaches a peak about halfway between the 0.135 and 0.140 s, and then it decays as the multiple reflections fade away. Thereafter, the LLW signal dominates and it is recognizable by the change in the shape of the waveform, from a square wave to a triangular wave.

Another method of suppressing the LLW signal is to increase the shear attenuation without changing the shear speed. Because the wave speeds are unchanged, this method produces orders of magnitude less discrepancy in the reflection/transmission coefficient but may not completely suppress the LLW signal. The reflected acoustic signal from ice with 10 times the shear attenuation, in dB per wavelength, is shown as (c), along with the difference $(a - c)$ in Fig. 5(d). The later part of $(a - c)$ is practically identical to that of $(a - b)$ indicating that the LLW signal is well suppressed in (c). An estimate of the UA is obtained by subtracting (c) from (b).

The difference $(a - c)$, which is relatively free of UA, is used to generate the LLW signal spectrogram shown in Fig. 5(c), and the signal spectrum (solid red curve) in Fig. 6(a). The LLW resonances B, C and D from Fig. 5(a) are clearly visible in Fig. 6(a). There are a number of additional but smaller spectral peaks present as well. Another simulation was run, in which the compressional and shear wave attenuations in the ice were set to zero, shown as the dotted curve in Fig. 6(a), in order to identify any spectral peaks that were suppressed by the wave attenuation. It is evident that the spectral peaks above 2 kHz were significantly suppressed by the attenuation within the ice. The values of attenuation in Table I are found in the published literature and represent the best estimate currently available.

III. LAMB WAVES

The equations of propagating waves in an elastic plate were derived by Professor Horace Lamb of Manchester University in 1917 (Lamb, 1917). Two modes were identified: symmetrical and asymmetrical. In the symmetric modes, the top and bottom surfaces of the elastic plate move in opposite directions. Conversely, in the asymmetric modes, the top and bottom surfaces move in the same direction. They satisfy the following equations.

For symmetric modes,

$$\frac{tanh(P)}{tanh(Q)} - \frac{X}{Y} = 0 \tag{2}$$

For asymmetric modes,

$$\frac{tanh(P)}{tanh(Q)} - \frac{Y}{X} = 0 \tag{3}$$

The intermediate variables, P, Q, X and Y are defined by the compressional (longitudinal) and shear wave speeds, V_L and V_S, of the elastic material, the thickness d of the elastic plate, and the speed and frequency of the Lamb wave, V and f, respectively, as follows,

$$P = \beta\frac{d}{2};\ Q = \alpha\frac{d}{2};\ X = 4\xi^2\alpha\beta;\ Y = (\xi^2 + \beta^2)^2 \tag{4}$$

$$\alpha = \xi(1 - (\frac{V}{V_L})^2)^{\frac{1}{2}};\ \beta = \xi(1 - (\frac{V}{V_S})^2)^{\frac{1}{2}};\ \xi = \frac{2\pi f}{V} \tag{5}$$

These equations are difficult to solve but numerical solutions for specific values of the elastic plate properties may be computed. The approach adopted is to keep V_L, V_S, d, and V constant, and plot the magnitude of the left-hand-side (LHS) of Eq. (2) and Eq. (3) as a function of f in order to search for the frequencies where it goes to zero. An example, where V=17,000 m/s is shown in Fig. 6(b).

A high value of V was chosen to ensure that it is supersonic in water, because only supersonic Lamb waves may radiate sound into the water. Lamb waves are to be found

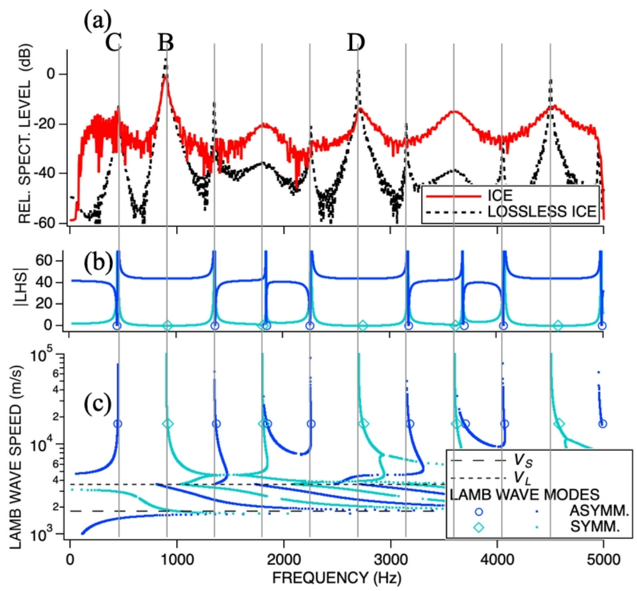

FIG. 6. (a) Spectrum levels of the isolated leaky Lamb wave signal from the ice in solid red, and an equivalent but lossless ice in dotted black. These were obtained by subtracting OASES simulations with enhanced shear attenuation from that of ice with the proper wave speeds and attenuations. (b) Plots of the | LHS | of Eq. (2) and Eq. (3) at V=17,000 m/s. (c) Traces of | LHS | =0 in (V, f) space, for symmetric and asymmetric modes. (color online).

where the magnitudes of the LHS of Eq. (2) and Eq. (3) go to zero, as marked by the small circles in Fig. 6(b). This process may be repeated for a wide range of values of V, and the positions of the zeroes trace out a dispersion diagram of all the Lamb waves predicted by the two equations, as shown in Fig. 6(c). For Lamb wave speeds greater than about 50,000 m/s, the dispersion curves tend to be vertical, and the frequencies do not change significantly. Below this speed, the dispersion curves are more complicated with numerous discontinuities. Some of the discontinuities appear to be connected to the wave speeds V_L and V_S, as shown in Fig. 6(c). At these speeds, the values of α and β in Eq. (5) pass through zero and change from real to imaginary. It is evident that the spectral peaks in Fig. 6(a) obtained from the OASES simulation coincide with the frequencies of the Lamb waves, as the Lamb waves' speeds tend asymptotically to infinity in Fig. 6(c), consistent with the downward radiation condition in Eq. (1), not just at B, C and D but also at lower peaks which in practice would be unlikely to be detected. In summary, the resonances in an ULS signal are predicted by the Lamb wave equations as the Lamb wave speed V asymptotically tends to infinity.

By restricting our attention to this asymptotic case, Eq. (2) to Eq. (5) can be greatly simplified. Setting V to infinity, and assuming that V_S is greater than zero, they reduce to:

For symmetric modes,

$$sin(\pi f \frac{d}{V_S}) = 0;\ f = N\frac{V_S}{d}; \qquad cos(\pi f \frac{d}{V_L}) = 0;\ f = (\frac{1}{2} + N)\frac{V_L}{d}; \tag{6}$$

For asymmetric modes,

$$cos(\pi f \frac{d}{V_S}) = 0;\ f = (\frac{1}{2} + N)\frac{V_S}{d}; \qquad sin(\pi f \frac{d}{V_L}) = 0;\ \ f = N\frac{V_L}{d} \tag{7}$$

In Eq. (6) and Eq. (7), N is an integer (N=1,2,3...). Using the values for d, V_S and V_L from Table I, Eq. (6) and Eq. (7) predict that the LLW signal frequencies are 900, 1800 Hz and so on for the symmetric modes, and 450, 1350 Hz and so on for the asymmetric modes. These values are very close to the spectral peaks observed in the simulated signals in Fig. 6(a). At approximately 1800 Hz, there is both a symmetric mode dependent on V_S from Eq. (6) and an asymmetric mode dependent on V_L from Eq. (7). Since the compressional wave speed is exactly twice the shear speed, the V_S and V_L dependent spectral peaks are not separable.

To separate the V_S and V_L dependent spectral peaks, another simulation was run with the shear speed and ice thickness set to 2700 m/s and 3 m, respectively. All the other parameters remain as stated in Table I. The result is shown in Fig. 7. This combination of shear speed and thickness produces spectral peaks that are dependent on V_S at the same frequencies as before, because the value of $\frac{V_S}{d}$ remains unchanged, but the spectral peaks that are dependent on V_L are displaced. The first peak dependent on V_S occurs at 450 Hz. The next peak at 600 Hz is dependent on V_L. The largest spectral peak, at 1800 Hz, occurs where the V_S and V_L dependent modes coincide and add constructively. At 3600 Hz, they again coincide but they appear to add destructively, and the peak is greatly diminished. It is noted that the V_L dependent modes are very weak, consistent with the finding in the Appendix. This example illustrates the potential of the ULS for probing the values of both V_S and V_L in the ice, but it is not a simple process to unravel them. That process is beyond the scope of this paper, but it will be pursued in a later study.

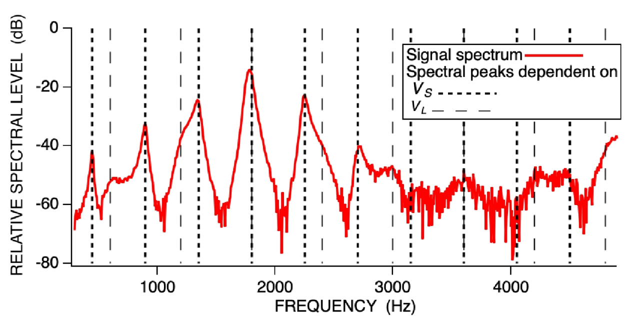

FIG. 7. Spectrum level of LLW signal at $V_S = 2700$ m/s and $d = 3$ m, all other parameters as stated in Table I (color online).

The above example is a rather contrived example because the shear speed of ice rarely exceeds 2000 m/s. Its purpose is to show that there may be spectral peaks associated with the compressional speed, as well as the shear wave speed. Williams and Francois (Williams and Francois, 1992) provide an expression for the shear speed in fresh water ice as a function of temperature. The temperature of Arctic sea ice rarely dips below -25° C, and the corresponding maximum shear speed of fresh water ice is 2,080 m/s. But seawater ice contains brine pockets which reduce the effective shear modulus, therefore its shear speed is always less.

IV. ATTENUATION

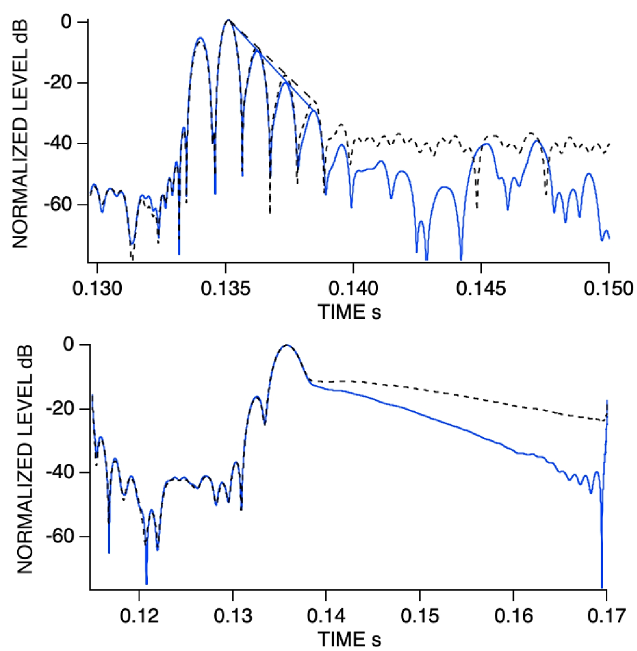

FIG. 8. Amplitude profiles of band passed signals from Fig. 4 of the specular reflections at 5 kHz (top) and the LLW signal at 919 Hz (bottom), compared to the lossless case (dashed curves), illustrating how compressional and shear wave attenuations influence the decay rates (color onine).

The influence of the attenuation of the compressional and shear waves in the ice may be observed in the simulations. The amplitude profiles of the highest frequency band in Fig. 4, which contains the specular reflections from the top and bottom interfaces (A), and the band at 919 Hz, which contains the LLW signal (B), are shown in Fig. 8. These are compared to the simulation where the attenuations a_L and a_S are set to zero (dashed curves). It is clearly seen that the decay rate of the peaks of the multiple reflections in the top panel is influenced by the compressional wave attenuation. Straight lines may be fitted through the peak amplitudes as shown. Similarly, the decay rate of the LLW signal is influenced by the attenuation of the shear wave. In this case, the decay rate is more complicated than a simple straight line. The difference between the lossy and lossless decay rates is greater in the LLW signal because the shear wave attenuation is significantly greater than that of the compressional wave. These results illustrate that an inversion process to extract the attenuations is feasible.

V. ROUGH INTERFACE

In this section, the effect of a rough interface between water and ice is explored. The finite element code SPECFEM2D (Cristini and Komatitsch, 2012) is better suited for simulating a rough interface than OASES. However, it is very computationally intensive and the computation load increases approximately as the third power of frequency. In studying rough surface scattering, it is necessary to generate several random realizations in order to obtain meaningful statistics. Therefore, the simulation was limited to frequencies below 1200 Hz, and the depth of the sonar was reduced to 50 m. Each run uses approximately 70,000 mesh elements, 52,000 time steps, and takes less than 7 minutes on a 48 processor node (TACC, 2022) of the Texas Advanced Computing Center (TACC).

To verify that SPECFEM2D delivers the expected results for a flat interface, the reflection from an infinitely thick sheet of ice was simulated, and presented as a spectrogram, as shown in Fig. 9(a). The spectrogram is scaled to show the reflection coefficient rather than the absolute signal spectral density as in Fig. 5. It shows a broad band response that is 6 dB below that of a perfect reflector due to the energy that penetrates the ice. Below 200 Hz, the response tapers away and some computation noise is noticeable. Above 1200 Hz (not shown) there is more computation noise due to the limitations of the mesh size. Next, the reflection from a 2 m thick sheet of ice with zero shear speed is shown in Fig. 9(b). The peak response shows a gain of 1 dB relative to a perfect reflector, due to multiple reflections in the ice sheet. The horizontal scale in Fig. 9(a) and (b) are expanded to show details within the main ridge. In (a) the ridge is straight and uniform. In (b) there is a slight kink at 900 Hz, coincident with $\frac{V_L}{2d}$, consistent with multiple reflections of the compressional wave, Eq. (6), and the OASES result in Fig. 5 (b).

The reflection from a 2 m thick sheet of ice with a shear speed of 1732 m/s is shown in Fig. 9(c). All other properties of the ice are as given in Table I. The response clearly shows two resonances: one at 816 Hz and the other at 411 Hz. They are 4 dB and 2 dB above that of a perfect reflector, respectively. The effect of changing the shear wave speed is shown in Fig. 10, in which shear speeds 1532, 1732 and 1932 m/s are compared. It is evident that the resonance frequencies change with the shear speed in the ice. The resonance frequencies are approximately in agreement with Eq. (6) and Eq. (7). The resonance connected with the compressional wave speed V_L at 900 Hz is still there but barely visible.

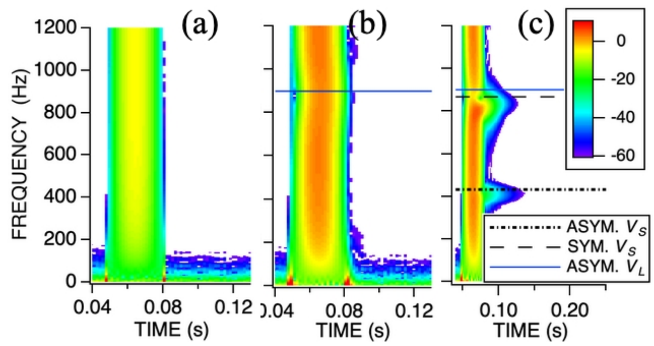

FIG. 9. Spectrograms of reflected signals, normalized by the reflection from a perfect reflector, from (a) an ice sheet of infinite thickness, (b) a 2 m thick ice with zero shear speed, and (c) a 2 m thick ice with a shear speed of 1732 m/s. All other properties as stated in Table I. The LLW frequencies predicted by Eqs. (5) and (6) are indicated by the horizontal lines. (color onine).

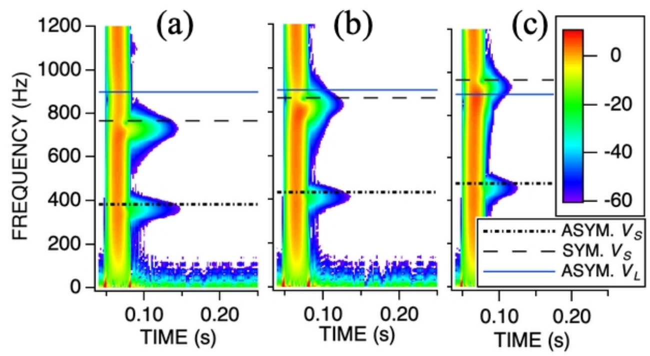

FIG. 10. Spectrograms of reflected signals, normalized by the reflection from a perfect reflector, from a 2 m thick ice sheet with shear speeds (a) 1532, (b) 1732 and (c) 1932 m/s. All other properties as stated in Table I. The frequencies predicted by Eq. (6) and Eq. (7) are shown as horizontal lines. (color onine).

The effect of a rough water-ice interface was simulated. The axially symmetric mode of the SPECFEM2D code is essentially a 3D model produced by revolving a 2D model about a chosen axis of symmetry. The roughness looks like the concentric grooves in a vinyl record.

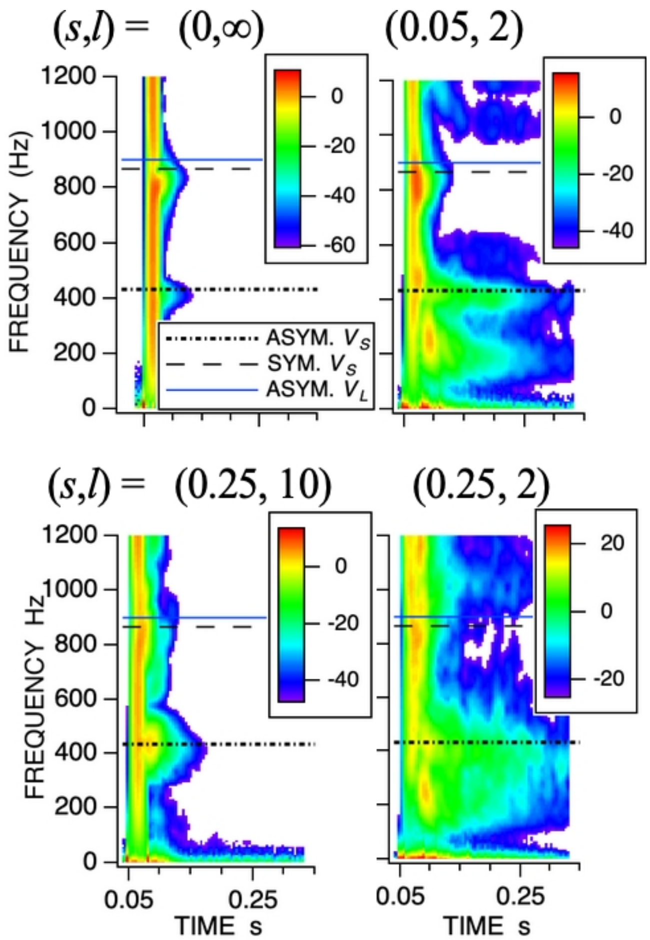

FIG. 11. Average spectrogram of reflected signals from 20 independent realizations of rough water-ice interfaces, under a 2 m thick ice sheet with Gaussian roughness of RMS height and correlation length (s,l). The air-ice interface is smooth. (color onine).

It cannot replicate a fully 3D model, but there is a possibility that the statistics of the scattered signal could be a useful proxy. There have been studies in which a compensation or correction factor has been put forward to allow a 2D model to be a proxy for a 3D model (Tran *et al.*, 2013). It was done for pressure-release, isotropic, rough surfaces and for a limited range of grazing angles. The correction factor was found to vary depending on a number of input parameters, but it was usually only a few decibels. Therefore, it would not be unreasonable to expect that the results of the cylindrically symmetric model to be equivalent to a 3D simulation for isotropic rough surfaces within a few decibels.

The roughness was modeled as a Gaussian random process with defined values of the RMS height and correlation length (s,l). The correlation length is defined as the distance at which the correlation becomes negligible. Starting at the axis of symmetry, on which the sonar is located, the z-coordinate of points on the rough interface, at radial distances l m apart, were assigned random values generated by a Gaussian random number generator, at the desired RMS deviation, s m. The correlation coefficient between these points should be zero by definition, since each random number produced by the random number generator is uncorrelated with any other. The points in between are filled in by a smooth interpolation algorithm that is internal to the SPECFEM2D code to produce a mesh that is consistent with the requirements of the finite element solver. The ice-air interface is kept flat, although it too can be made rough, since SPECFEM2D can simulate multiple rough interfaces. Twenty random realizations were used to produce each average spectrogram. The average spectrograms are shown in Fig. 11. Flat ice is indicated by (0,∞). At (0.05,2), the resonance peaks were broadened and there was an enhancement of the signal level compared to the corresponding flat interface. The reverberation tail also extended over a longer time. An additional resonance peak due to the roughness appeared at a frequency of 244 Hz and a delay of 0.094 s. It appears to have caused the LLW peak at 411 Hz to be shifted to 465 Hz. Keeping the ratio of RMS roughness to correlation length constant, the next set of simulations at (0.25,10), showed a further broadening of the resonance peaks, but a reduction in the reverberation tail. Finally, keeping the same RMS roughness but reducing the correlation length back to 2, at (0.25,2), the resonance peaks are smeared beyond recognition. These simulations illustrate that roughness, depending on its severity, can enhance or disrupt the LLW signal. Both the RMS roughness and its correlation length are important. Future studies will explore the effects of roughness in greater detail.

While the cylindrical symmetric geometry has its limitations, it is possibly the most readily useful model under the present circumstances, for the following reasons: (1) It is a 3D scattering model that is physically correct. Unlike perturbation theory, the small slope approximation, the Kirchhoff approximation, or any other approximation, nothing is neglected. All orders of scattering and multiple scattering are implicitly included. (2) It is a simple model that has just two simple variables, the RMS roughness and the correlation length. Although it would be preferable to fully represent the fine-scale roughness of the underside of the ice in 3D and apply an appropriate scattering calculation to predict the effects of roughness, that goal is still a long way off. (3) The fine-scale 3D roughness of the underside of ice is unknown. One of the more recent publications is (Wadhams, 2012), in which an EM2000 multibeam sonar was used to map the underside of the ice. It shows large scale features, such as ridges and protrusions in an otherwise featureless and apparently flat interface. The EM2000 has a bandwidth of 5.3 kHz, which corresponds to a resolution of 0.3 m at best. The finite element simulations show that a roughness of just 0.05 m RMS can significantly disrupt the signal structure, and that higher-resolution measurements will be needed

VI. CONCLUSIONS

It is demonstrated that the mechanical properties of the Arctic ice sheet may have a measurable effect on the underwater acoustic reflection, as measured by an upward-looking sonar. At a sufficiently high frequency and bandwidth, the reflections from the top and bottom interfaces of the ice are separable, yielding the compressional wave travel time through the ice, which is equal to the thickness-to-compressional wave speed ratio. In addition, there are resonances that may be extracted from the reflected signal that are governed by the shear speed-to-thickness ratio, and in some cases the compressional wave speed-to-thickness ratio. The resonance phenomenon is directly related to Lamb waves, particularly leaky Lamb waves. These are Lamb waves that reradiate acoustic energy back into the water. In order to do so, they must be supersonic relative to the wave speed in water, and a relatively simple solution is obtained by setting the Lamb wave speed to infinity in the Lamb wave equations. The process of unraveling the spectral peaks and the ratios that they represent is expected to require further development. It is also shown that the inversion for the attenuation of both the compressional and shear waves in the ice is feasible. The ice-water interface is known to be rough, and it can have a disruptive effect on the resonances, depending on the severity. Simulations with a finite element model were used to explore a few cases of roughness effects in order to get an estimate of roughness levels that may be tolerated. This too is to be studied in greater detail.

ACKNOWLEDGMENTS

Nicholas Chotiros was funded by the US Office of Naval Research, Code 32 Ocean Acoustics Program, Grant N00014-20-1-2041, Gaye Bayrakci and Angus Best were funded by the UK Defence and Security Accelerator (DASA), Grant ACC2016927. The authors acknowledge the Texas Advanced Computing Center (TACC) at The University of Texas at Austin for providing high performance computing (HPC) resources that have contributed to the research results reported within this paper. The authors acknowledge the assistance of Paul Cristini in getting the SPECFEM2D up and running on the HPC.

Appendix

Proof that resonance frequencies as observed in an ULS are the same for a plate in contact with water on one side as for a plate in a vacuum

The dispersion equation for a plate in a vacuum from Yu and Tian (Yu and Tian, 2015) is reproduced here,

$$\begin{bmatrix} k_S^2-\xi^2 & k_S^2-\xi^2 & -2k_S\xi & 2k_S\xi \\ 2k_L\xi & -2k_L\xi & k_S^2-\xi^2 & k_S^2-\xi^2 \\ (k_S^2-\xi^2)g_L & \frac{k_S^2-\xi^2}{g_L} & -2k_S\xi g_S & \frac{2k_S\xi}{g_S} \\ 2k_L\xi g_L & \frac{-2k_L\xi}{g_L} & (k_S^2-\xi^2)g_S & \frac{k_S^2-\xi^2}{g_S} \end{bmatrix} = y_v = 0$$

where $g_L = e^{ik_L d}$, $g_S = e^{ik_S d}$, $k_L^2 = \frac{\omega^2}{V_L^2} - \xi^2$, $k_S^2 = \frac{\omega^2}{V_S^2} - \xi^2$, $\omega = 2\pi f$, and $\xi = \frac{2\pi f}{V}$. V_L and V_S are the compressional and shear wave speeds in the ice, d is the ice thickness, and ξ is the wavenumber of the Lamb wave. In the case of a Lamb wave that radiates acoustic energy in the vertically downward direction, the wavenumber tends to zero. Setting ξ to zero and taking the magnitude of the matrix, with the aid of LiveMath symbolic software (MathMonkeys, 2003), the following result is obtained,

$$-\frac{k_S^8}{g_L g_S}(g_S+1)(g_S-1)(g_L+1)(g_L-1) = |y_v|_{\xi=0} = 0. \tag{8}$$

This solution is identical to Eq. (6) and Eq. (7), which is as expected. $g_S - 1 = 0$ when $f = N\frac{V_S}{d}$, $g_S + 1 = 0$ when $f = (\frac{1}{2} + N)\frac{V_S}{d}$, etc.

The dispersion equation for a plate in contact with water on one side from Yu and Tian (Yu and Tian, 2015) is also reproduced here,

$$\begin{bmatrix} k_S^2-\xi^2 & k_S^2-\xi^2 & -2k_S\xi & 2k_S\xi & 0 \\ 2k_L\xi & -2k_L\xi & k_S^2-\xi^2 & k_S^2-\xi^2 & 0 \\ (k_S^2-\xi^2)g_L & \frac{k_S^2-\xi^2}{g_L} & -2k_S\xi g_S & \frac{2k_S\xi}{g_S} & \frac{\omega^2\rho_w}{\mu} \\ 2k_L\xi g_L & \frac{-2k_L\xi}{g_L} & (k_S^2-\xi^2)g_S & \frac{k_S^2-\xi^2}{g_S} & 0 \\ k_L g_L & \frac{-k_L}{g_L} & -\xi g_S & \frac{-\xi}{g_S} & \gamma \end{bmatrix} = y_w = 0$$

where the shear speed in the ice V_S is related to the ice shear modulus μ and density ρ by $V_S^2 = \frac{\mu}{\rho}$. In the water, ρ_w, and c_o are the density and sound speed of water and $\gamma^2 = \frac{\omega^2}{c_o^2} - \xi^2$. As before, ξ is set to zero and the magnitude of the matrix reduces to,

$$-\frac{\gamma k_S^8}{g_L g_S}(g_S+1)(g_S-1)[(g_L+1)(g_L-1) - \frac{\rho_w c_o}{\rho V_L}(g_L^2+1)] = |y_w|_{\xi=0} = 0. \tag{9}$$

It is noted that the terms $(g_S+1)(g_S-1)$ in Eq. (9) are exactly the same as in Eq. (8) for the plate in a vacuum, which indicates that the resonance frequencies that depend on V_S are unchanged. The terms $(g_L+1)(g_L-1)$ are also present in Eq. (9) as in Eq. (8) but there is an additional term, which means that the resonances that are dependent on V_L are modified. Given typical values of the sound speeds and densities of water and ice, numerical calculations (not shown) show that the term in the square brackets in Eq. (9) has minima at the same frequencies as in Eq. (8) for the plate in a vacuum, but the minima do not reach zero, indicative of possibly weaker resonances, but at the same frequencies.

Author Declarations

There are no conflicts to disclose.

Data Availability

The data that support the findings of this study are available from the corresponding author upon reasonable request.

References

Cegla, F. B., Cawley, P., and Lowe, M. J. S. (**2005**). "Material property measurement using the quasi-scholte mode - a waveguide sensor," J. Acoust. Soc. Am. **117**(3), 1098–1107, doi: 10.1121/1.1841631.

Cristini, P., and Komatitsch, D. (**2012**). "Some illustrative examples of the use of a spectral-element method in ocean acoustics," J. Acoust. Soc. Am. **131**(3), EL229–EL235, doi: 10.1121/1.3682459.

Discovery of Sound in the Sea (**2023**). "What are common underwater sounds?" https://dosits.org/science/sounds-in-the-sea/what-are-common-underwater-sounds/.

Georgiades, E., Lowe, M. J. S., and Craster, R. V. (**2022**). "Leaky wave characterisation using spectral methods," The Journal of the Acoustical Society of America **152**(3), 1487–1497, doi: 10.1121/10.0013897.

Hobaek, H., and Sagen, H. (**2016**). "On underwater sound reflection from layered ice sheets," in *39th Scandinavian Symposium on Physical Acoustics*.

Lamb, H. (**1917**). "On waves in an elastic plate," Proceedings of the Royal Society, Series A **93**(648), 114–128, https://www.jstor.org/stable/93792.

Landy, J. C., Dawson, G. J., Tsamados, M., Bushuk, M., Stroeve, J. C., Howell, S. E. L., Krumpen, T., Babb, D. G., Komarov, A. S., Heorton, H. D. B. S., Belter, H. J., and Aksenov, Y. (**2022**). "A year-round satellite sea-ice thickness record from cryosat-2," Nature **609**(7927), 517–522, https://doi.org/10.1038/s41586-022-05058-5, doi:

10.1038/s41586-022-05058-5.

MathMonkeys (**2003**). "Theorist reference manual" https://www.livemath.com/documentation/Theorist-ReferenceManual-v2.0.pdf.

McCammon, D. F., and McDaniel, S. T. (**1985**). "The influence of the physical properties of ice on reflectivity," J. Acoust. Soc. Am. **77**(2), 499–507, doi: 10.1121/1.391869.

Moreau, L., Boué, P., Serripierri, A., Weiss, J., Hollis, D., Pondaven, I., Vial, B., Garambois, S., Larose, É., Helmstetter, A., Stehly, L., Hillers, G., and Gilbert, O. (**2020**). "Sea ice thickness and elastic properties from the analysis of multimodal guided wave propagation measured with a passive seismic array," Journal of Geophysical Research: Oceans **125**(4), doi: 10.1029/2019jc015709.

Moreau, L., Lachaud, C., Thery, R., Predoi, M. V., Marsan, D., Larose, E., Weiss, J., and Montagnat, M. (**2017**). "Monitoring ice thickness and elastic properties from the measurement of leaky guided waves: A laboratory experiment," J. Acoust. Soc. Am. **142**(5), 2873, https://www.ncbi.nlm.nih.gov/pubmed/29195456, doi: 10.1121/1.5009933.

Roper, D., Harris, C. A., Salavasidis, G., Pebody, M., Templeton, R., Prampart, T., Kingsland, M., Morrison, R., Furlong, M., Phillips, A. B., and McPhail, S. (**2021**). "Autosub long range 6000: A multiple-month endurance auv for deep-ocean monitoring and survey," IEEE Journal of Oceanic Engineering **46**(4), 1179–1191, doi: 10.1109/joe.2021.3058416.

Schmidt, H. (**2011**). "Oases version 3.1: User guide and reference manual," Technical Report, https://acoustics.mit.edu/faculty/henrik/oases.pdf.

Serripierri, A., Moreau, L., Boué, P., Weiss, J., and Roux, P. (**2022**). "Recovering and monitoring the thickness, density, and elastic properties of sea ice from seismic noise recorded in svalbard," The Cryosphere **16**(6), 2527–2543, doi: 10.5194/tc-16-2527-2022.

TACC (**2022**). "Texas advanced computing center , Stampede2 user guide," Technical Report, https://www.tacc.utexas.edu/systems/stampede2.

Tran, B., Joshi, S., and Isakson, M. J. (**2013**). "Applicability of two-dimensional boundary scattering models as a proxy for three-dimensional models," **19**, 070079, doi: 10.1121/1.4800511.

Wadhams, P., Wilkinson, J. P., and McPhail, S. D. (**2006**). "A new view of the underside of arctic sea ice," Geophysical Research Letters **33**(4), doi: 10.1029/2005gl025131.

Wadhams, P. (**2012**). "The use of autonomous underwater vehicles to map the variability of under-ice topography," Ocean Dynamics **62**(3), 439–447, doi: 10.1007/s10236-011-0509-1.

Weeks, W., and Assur, A. (**1967**). *The Mechanical Properties of Sea Ice* (Cold Regions Research and Engineering Laboratory, U. S. Army Materiel Command, Hanover, NH, U. S. A.).

Williams, K. L., and Francois, R. E. (**1992**). "Sea ice elastic moduli: Determination of Biot parameters using in-field velocity measurements," J. Acoust. Soc. Am. **91**(5), 2627–2636.

Yu, L., and Tian, Z. (**2015**). "Case study of guided wave propagation in a one-side water-immersed steel plate," Case Studies in Nondestructive Testing and Evaluation **3**, 1–8, doi: 10.1016/j.csndt.2014.11.001.